SCIENCE CHINA
Chemistry

•ARTICLES•

https://doi.org/10.1007/s11426-019-9618-7

Side chain engineering of quinoxaline-based small molecular nonfullerene acceptors for high-performance poly(3-hexylthiophene)-based organic solar cells

Bo Xiao[1,2†], Qianqian Zhang[1,3†], Gongqiang Li[3*], Mengzhen Du[1,3], Yanfang Geng[1*], Xiangnan Sun[1,2], Ailing Tang[1], Yingliang Liu[4], Qiang Guo[4] & Erjun Zhou[1,2,4*]

[1]*CAS Key Laboratory of Nanosystem and Hierarchical Fabrication, CAS Center for Excellence in Nanoscience, National Center for Nanoscience and Technology, Beijing 100190, China;*
[2]*Center of Materials Science and Optoelectronics Engineering, University of Chinese Academy of Sciences, Beijing 100049, China;*
[3]*Key Laboratory of Flexible Electronic (KLOFE) & Institute of Advanced Materials (IAM), Jiangsu National Synergistic Innovation Center for Advanced Materials (SICAM), Nanjing Tech University (Nanjing Tech), Nanjing 211816, China;*
[4]*Henan Institutes of Advanced Technology, Zhengzhou University, Zhengzhou 450003, China*

Received August 30, 2019; accepted September 19, 2019; published online December 11, 2019

Poly(3-hexylthiophene) (P3HT) is one of the most used semiconducting polymers for organic photovoltaics because it has potential for commercialization due to its easy synthesis and stability. Although the rapid development of the small molecular non-fullerene acceptors (NFAs) have largely improved the power conversion efficiency (PCE) of organic solar cells (OSCs) based on other complicated p-type polymers, the PCE of P3HT-based OSCs is still low. In addition, the design principle and structure-properties correlation for the NFAs matching well with P3HT are still unclear and need to be investigated in depth. Here we designed a series of NFAs comprised of acceptor (A) and donor (D) units with an A_2-A_1-D-A_1-A_2 configuration. These NFAs are abbreviated as **Qx3**, **Qx3b** and **Qx3c**, where indaceno[1,2-*b*:5,6-*b′*]dithiophene (IDT), quinoxaline (Qx) and 2-(1,1-dicyanomethylene)rhodanine serve as the middle D, bridged A_1 and the end group A_2, respectively. By subtracting the phenyl side groups appended on both IDT and Qx skeletons, the absorption spectra, energy levels and crystallinity could be regularly modulated. When paired with P3HT, three NFAs show totally different photovoltaic performance with PCEs of 3.37% **(Qx3)**, 6.37% **(Qx3b)** and 0.03% **(Qx3c)**, respectively. From **Qx3** to **Qx3b**, the removing of phenyl side chain in the middle IDT unit results in the increase of crystallinity and electron mobility. However, after subtracting all the grafted phenyl side groups on both IDT and Qx units, the final molecule **Qx3c** exhibits the lowest PCE of only 0.03%, which is mainly attributed to the serious phase-separation of the blend film. These results demonstrate that optimizing the substituted position of phenyl side groups for A_2-A_1-D-A_1-A_2 type NFAs is vital to regulate the optoelectronic property of molecule and morphological property of active layer for high performance P3HT-based OSCs.

P3HT, non-fullerene acceptor, phenyl, quinoxaline, organic solar cells

---

Citation: Xiao B, Zhang Q, Li G, Du M, Geng Y, Sun X, Tang A, Liu Y, Guo Q, Zhou E. Side chain engineering of quinoxaline-based small molecular nonfullerene acceptors for high-performance poly(3-hexylthiophene)-based organic solar cells. *Sci China Chem*, 2019, 62, https://doi.org/10.1007/s11426-019-9618-7

---

†These authors contributed equally to this work.
*Corresponding authors (email: iamgqli@njtech.edu.cn; gengyf@nanoctr.cn; zhouej@nanoctr.cn)

1 Introduction

Organic solar cells (OSCs) possess several advantages such as low-cost, light weight and flexibility, and thus attract immense attention in recent decades [1–5]. Thanks to the emergence of diverse promising p-type and n-type organic semiconductors, the power conversion efficiency (PCE) of OSCs has been rapidly enhanced from 4%–5% in 2005 [6] to over 16% in 2019 [7]. However, with the purpose of pursuing good light-harvesting and suitable electron-donating capability, the chemical structures of p-type polymers become more and more complicated [8], which would lead to inevitable problems such as high cost and bad reproducibility. Poly(3-hexylthiophene) (P3HT), by contrast, is a good choice to promote the commercialization of OSCs technology as a simple photovoltaic polymer [9]. However, because of the high-lying HOMO (highest occupied molecular orbital) energy level (~−5.0 eV) [10] and band gap of 1.9 eV, P3HT could only realize a low open-circuit voltage (V_{OC}) of ~0.6 V, short-circuit current (J_{SC}) of ~10 mA/cm^2 and PCE of ~5% when blending with PC$_{61}$BM. The highest PCE of P3HT-based solar cells increased to 7.40% by using a kind of complicated indene bisadduct of fullerene derivative (IC$_{70}$BA) as early as 2012 [11], but it is at a standstill in recent years due to the difficulty to fine-tune the properties of fullerene.

As a generation of promising electron-accepting materials, the small molecular non-fullerene acceptors (NFAs) came into being as research hotspots due to their advantages of well-defined molecular structure, easy modification, facile synthesis and purification [12−14]. In combination with many excellent polymer donors, a single-junction OSC displayed an outstanding PCE over 16% [7], benefiting from the rapid development of NFAs, such as Y6 [15−17]. Compared with the achievements of other polymer donors, there is still a huge potential to develop high-performance P3HT-based OSCs. The reported NFAs combining with P3HT have mainly used fluorine [18,19], carbazole [20], dibenzosilole [21], or bifluorenylidene [22], spirobifluorene [23−25], indeno[2,1-*a*]fluorine [26], and indaceno [1,2-*b*:5,6-*b'*]dithiophene (IDT) [27−32] as the central core. Among them, IDT-based A$_2$-A$_1$-D-A$_1$-A$_2$ type NFAs demonstrate the best photovoltaic performance, where the bridged A$_1$ groups are mostly confined to benzothiadiazole (BT) and benzo[*d*][1,2,3]triazole (BTA) segments (as shown in Scheme 1). The A$_2$-BT-IDT-BT-A$_2$ type small molecules with different end-capped groups could achieve high J_{SC} and PCE, such as IDT-2BR (V_{OC}=0.84 V; J_{SC}=8.91 mA/cm^2; PCE=5.12% [27]), BT2b (V_{OC}=0.92 V; J_{SC}=10.02 mA/cm^2; PCE=6.08% [33]) and O-IDTBR (V_{OC}=0.72 V; J_{SC}=13.9 mA/cm^2; PCE=6.4% [28]). On the other hand, A$_2$-BTA-IDT-BTA-A$_2$ based NFAs could realize high V_{OC} of PCE, such as BTA1 (V_{OC}=1.02 V, J_{SC}=7.37 mA/cm^2, PCE=5.12% [29]), BTA2 (V_{OC}=1.22 V, J_{SC}=6.15 mA/cm^2, PCE=4.50% [30]) and BTA3 (V_{OC}=0.90 V, J_{SC}=9.64 mA/cm^2, PCE=5.64% [34]). Therefore, A$_2$-A$_1$-D-A$_1$-A$_2$ type NFAs can match well with P3HT and it is also vital to develop new electron-withdrawing A$_1$ unit besides BT and BTA.

From the viewpoint of chemical structure, Qx unit is also a kind of benzene-based electron-deficient two-membered aromatic ring [35–37], similar with BT and BTA. Qx exhibits medium electron-withdrawing ability between BT and BTA (BT>Qx>BTA) [28,29,38] and also provides the possibility of introducing different substituents on the 2- and 3-positions. Thus, Qx has been widely utilized to construct p-type photovoltaic polymers with the highest PCE of 9.2% [39] and 11.7% [40] when blending with fullerene acceptor or NFA, repectively. However, the reports of Qx-based n-type photovoltaic materials are very limited. In 2014, Zhang *et al.* [41] synthesized a Qx modified C$_{60}$ derivative of TQMA and achieved a PCE of 2.8% when blending with P3HT. In 2018, we synthesized two Qx-based NFAs and named as Qx1 and Qx1b, where IDT and rhodanine were adopted as the central and terminal segment. OSCs based on P3HT:Qx1 and P3HT:Qx1b showed PCEs of 4.03% and 4.81%, respectively [39]. The priliminary results indicate that A$_2$-Qx-IDT-Qx-A$_2$ based materials are effective to match with P3HT, which also privides a chance to investigate the effect of side chains on both IDT and Qx units. Therefore, here we synthesized three NFAs and named as **Qx3**, **Qx3b** and **Qx3c**, respectively, where 2-(1,1-dicyanomethylene)rhodanine (RCN) was used as the end group A$_2$ and the molecular backbone was fixed to RCN-Qx-IDT-Qx-RCN (as shown in Scheme 1(b)). By adjusting the numbers of the aromatic side groups in both IDT an Qx, the optoelectronic properties of three NFAs could be fine-tuned.

The systematical studies of UV-vis absorption, photoluminescence (PL), cyclic voltammetry (CV), space charge limit current (SCLC) mobility, atomic force microscopy (AFM) and grazing incident wide-angle X-ray scattering (GIWAXS) revealed the strong relationship between aromatic side groups and molecular conformation, optoelectronic, morphological and photovoltaic properties. Firstly, the presence of eight phenyl groups attached to both IDT and Qx units decrease the crystallinity and electron mobility of **Qx3**, thus resulting in a low J_{SC} and PCE. Secondly, the removal of all the eight phenyl groups induces totally planar molecular conformation of **Qx3c**, which instead tends to form worse phase-separation, leading to much lower J_{SC} and fill factor (FF). The highest PCE of 6.37% was realized for **Qx3b** upon only taking away the phenyl side groups attached to the IDT units, which is one of the highest values for P3HT-based solar cells with non-fullerene acceptors. Our results demonstrate that side chain engineering play a vital role in A$_2$-A$_1$-D-A$_1$-A$_2$ type NFAs and indicate that Qx unit is an

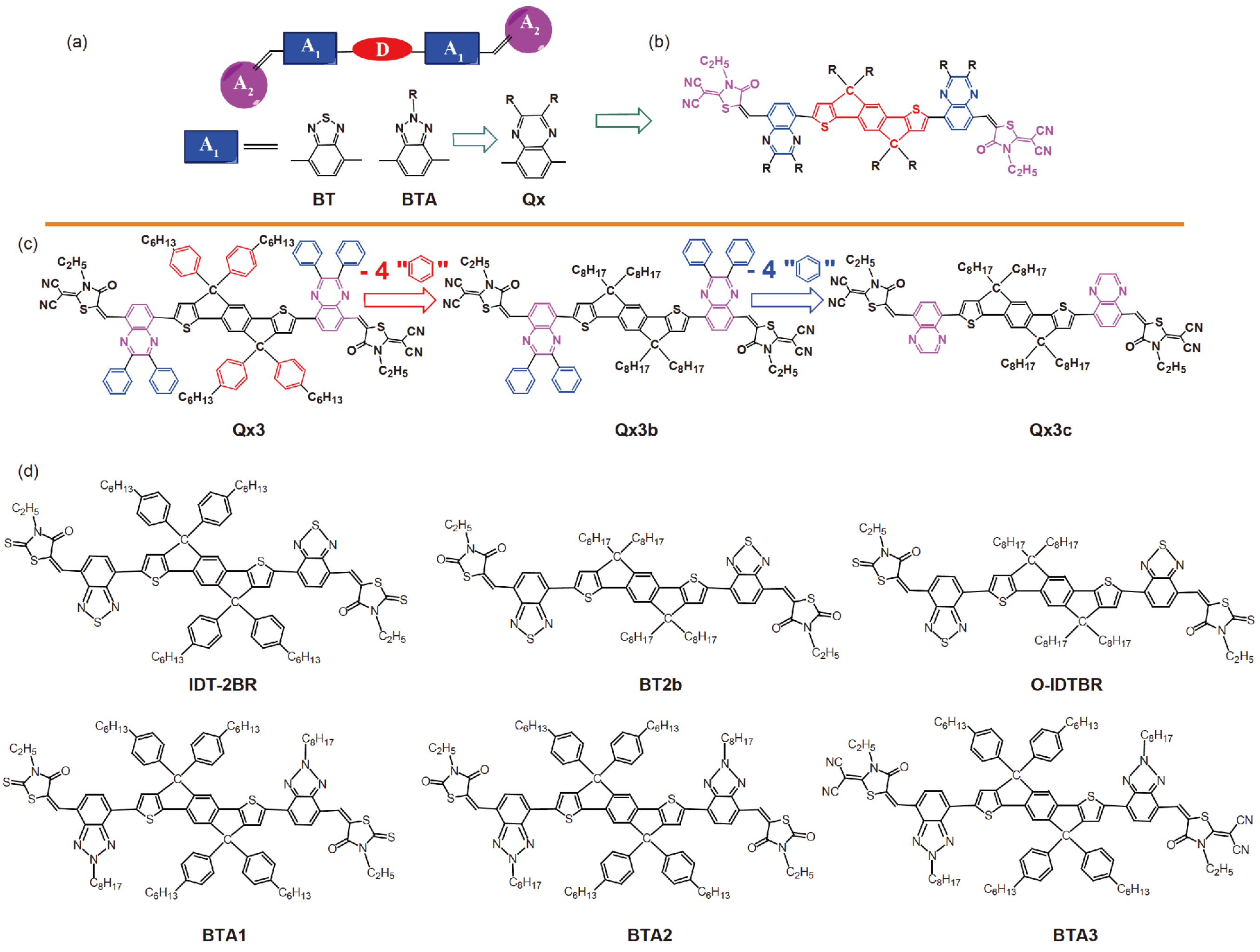

Scheme 1 (a) The A_2-A_1-D-A_1-A_2 type NFAs with BT, BTA and Qx as the bridged A_1 unit; (b) the general molecular backbone of RCN-Qx-IDT-Qx-RCN; (c) three specific chemical structures of Qx-based NFAs **Qx3**, **Qx3b** and **Qx3c**; (d) the structures of small molecule IDT-2BR, BT2b, O-IDTBR, BTA1, BTA2 and BTA3 (color online).

effective building block to construct NFAs to combine with P3HT.

2 Results and discussion

2.1 Synthesis of materials

To synthesize three RCN-Qx-IDT-Qx-RCN type NFAs, the most important intermidiates are 8-bromo-2,3-diphenylquinoxaline-5-carbaldehyde (intermediate 3) and 8-bromoquinoxaline-5-carbaldehyde (intermediate 5). Intermediate 3 could be easily synthesized by converting one bromine in 5,8-bromo-2,3-diphenylquinoxaline (intermediate 2) to aldehyde group, as shown in Scheme 2(a) (the route 1). However, the same method failed to synthesize intermediate 5, probably due to the high reactivity of H atoms in 2,3-position of quinoxaline with *n*-butyllithium (the route 2). Alternatively, the intermediate 5 could be obtained from 4-bromo-7-methylbenzo[*c*][1,2,5]thiadiazole by converting methyl group to aldehyde group (the route 3) [42]. Three small molecular acceptors, **Qx3**, **Qx3b** and **Qx3c**, were obtained through condensation reaction between di-aldehyde compounds and RCN, respectively, as shown in Scheme 1. The detailed synthesis procedure was shown in Supporting Information online. The structures of three NFAs were confirmed through nuclear magnetic resonance (NMR) and matrix-assisted laser desorption/ionization time of flight (MALDI-TOF) as shown in Figure S1 (Supporting Information online). The thermal gravimetric (TGA) analysis shown in Figure S2(a) reveals that **Qx3**, **Qx3b** and **Qx3c** possess good thermal stability with the deposition temperature up to 390, 385 and 365 °C, respectively, corresponding to 5% weight loss. In differential scanning calorimetry (DSC) spectra (Figure S2(b)), **Qx3** did not show any peaks at the first cooling and second rising. However, **Qx3b** and **Qx3c** exhibited the alkyl chains melting and backbone melting peaks at 282/311 °C and 208/299 °C, respectively. In addition, the exothermic peak

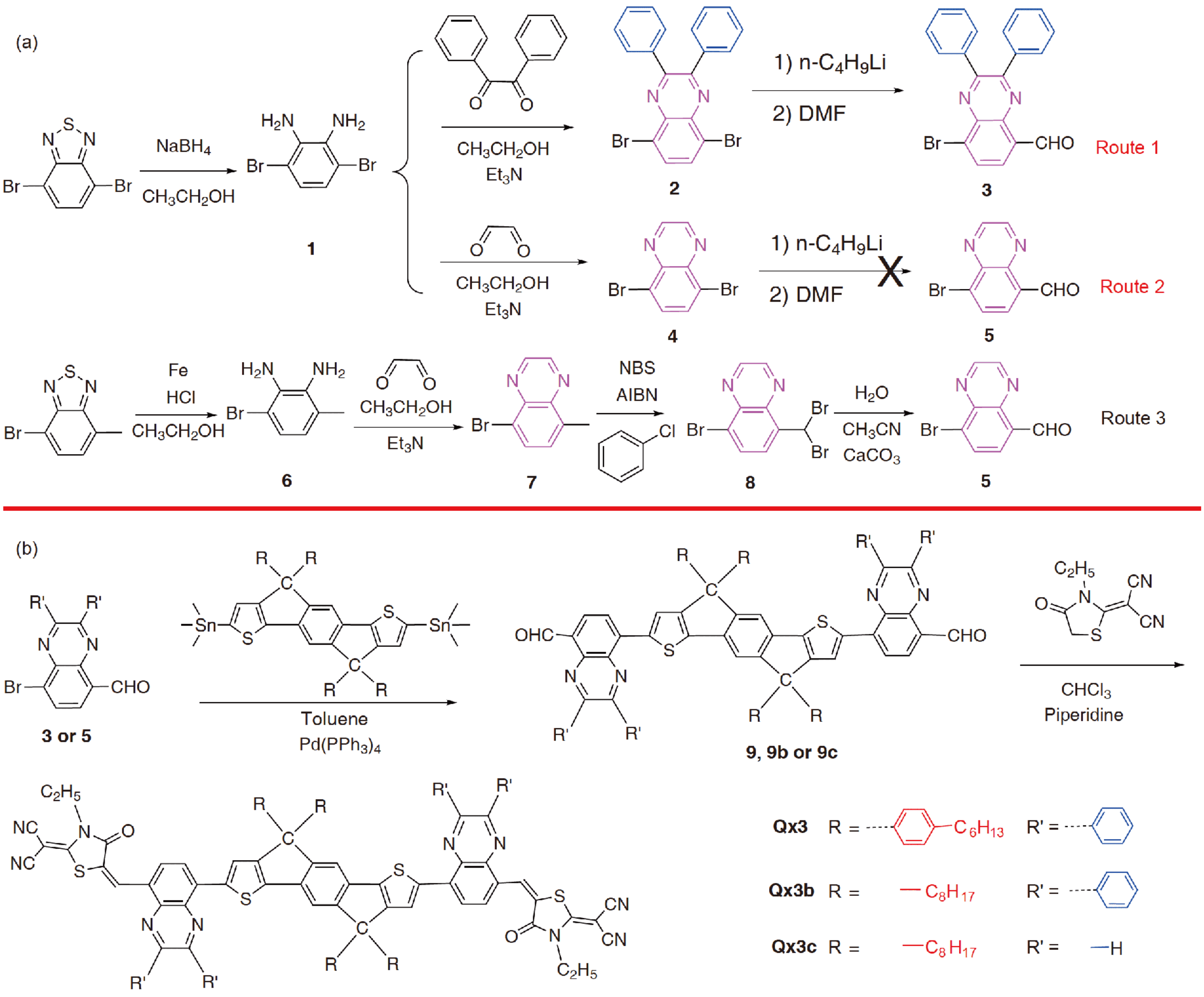

Scheme 2 (a) Synthetic routes for the intermidiates; (b) synthetic route of Qx-based small molecules **Qx3**, **Qx3b** and **Qx3c** (color online).

corresponding to recrystallization was observed in **Qx3b** (257 °C) and **Qx3c** (240 °C). These results indicate that **Qx3b** and **Qx3c** may adopt a better interchain packing than **Qx3**.

2.2 Characterization

The UV-vis absorption spectra of **Qx3**, **Qx3b** and **Qx3c** in chloroform solutions and in films are shown in Figure 1. In solution, they exhibit two similar absorption bands with the peak at ~400 and ~650 nm, respectively, which are assigned to the π-π^* and intramolecular charge transfer transition. **Qx3** shows an absorption maximum at 613 nm with an absorption coefficient of 1.03×10^5 L mol^{-1} cm^{-1}, while **Qx3b** and **Qx3c** show red-shifted maximum peaks at 642 and 636 nm as well as slightly higher absorption coefficient of 1.04×10^5 and 1.10×10^5 L mol^{-1} cm^{-1}, respectively. The absorption onsets of **Qx3c** and **Qx3b** in solution sequentially red-shift compared with **Qx3**. In the thin films, **Qx3** exhibits an absorption band from 500 to 750 nm with maximum at 654 nm, while **Qx3b** and **Qx3c** demonstrate red-shifted and fine-structured absorption band in the range from 450 to 800 nm, with two peaks at 706 and 686 nm, respectively, suggesting that the removal of phenyl side groups induced more planar conjugated backbone. **Qx3b** and **Qx3c** exhibit obvious shoulders near 650 nm, indicating that **Qx3b** and **Qx3c** possess a highly ordered molecular packing due to the intense intermolecular interactions compared with **Qx3**. In addition, **Qx3b** and **Qx3c** show more complementary absorption with donor P3HT than **Qx3**. The optical gaps of **Qx3**, **Qx3b** and **Qx3c** are estimated to be 1.64, 1.59 and 1.60 eV, respectively, from the absorption edges of their low-energy absorption bands. These results indicate that the adjustment of phenyl side groups on the IDT units has distinct effect on the absorption both in solution and thin film.

The electrochemical properties of **Qx3**, **Qx3b** and **Qx3c** were evaluated by cyclic voltammetry (CV) measurements as depicted in Figure 1(c), with thin films on a platinum plate in acetonitrile solution of 0.1 mol L^{-1} Bu_4NPF_6 (Bu=butyl) at scan rate of 50 mV s^{-1}. The lowest unoccupied molecular

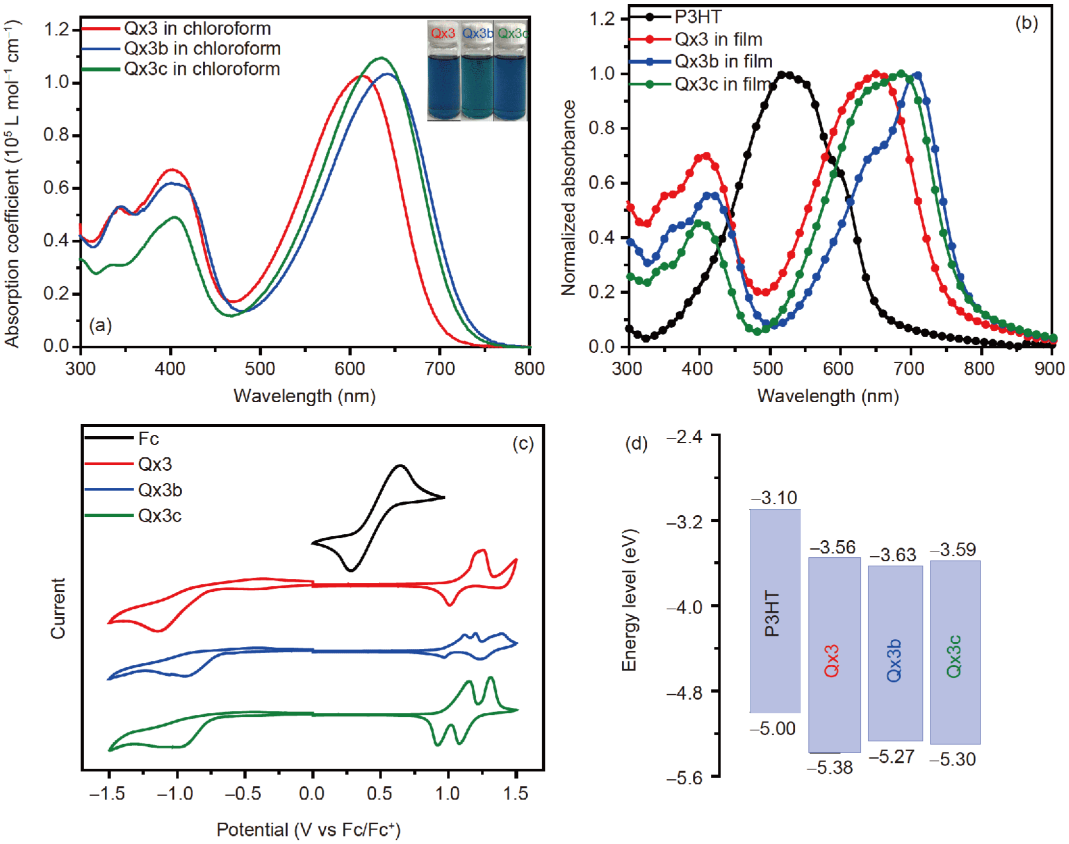

Figure 1 UV-vis absorption spectra of **Qx3**, **Qx3b** and **Qx3c** in chloroform solution (a) and thin film together with P3HT absorption in film (b). (c) CV curves of **Qx3**, **Qx3b** and **Qx3c**. (d) Molecular energy level diagrams of donor and acceptor obtained from CV measurements (color online).

orbitals (LUMO) and HOMO energy levels E_{LUMO} and E_{HOMO} are estimated according to the equation $E_{\mathrm{HOMO/LUMO}}=-e(E_{\mathrm{onset,ox/red}}+4.80\ \mathrm{eV})$ from the onset oxidation potential $E_{\mathrm{onset,ox}}$ and reduction potential $E_{\mathrm{onset,red}}$ and collected in Table 1. The $E_{\mathrm{HOMO/LUMO}}$ of **Qx3**, **Qx3b** and **Qx3c** is −5.38 eV/−3.56 eV, −5.27 eV/−3.63 eV and −5.30 eV/−3.59 eV, respectively. Thus, in comparison with **Qx3**, the removing phenyl groups both on IDT and Qx units cause LUMO energy level down-shift and HOMO energy level up-shift. Therefore, the electrochemical band gaps decrease, which is in accordance with the optical results. The results indicate that the phenyl side groups linking to both D and A_1 units have an influence on the molecular energy level of A_2-A_1-D-A_1-A_2 type NFAs, which may originate from the extent of molecular planarity. In addition, there is enough driving force for exciton dissociation between P3HT (−3.10 eV/−5.00 eV) and these NFAs.

We also performed density functional theory (DFT) calculations through Gaussian 09 at B3LYP/6-31G(*d*) level to visualize the chemical geometries and electronic properties of the prepared acceptors. Figure 2 shows the top view and side view of the minimum energy conformations of **Qx3**, **Qx3b** and **Qx3c**. After subtracting the phenyl groups attached to the IDT unit, the dihedral angle between the Qx and IDT as well as the Qx and the RCN in **Qx3b** is estimated to be 11° and 1.1°, respectively, which are slightly larger than those in **Qx3**. The dihedral angles between the phenyl unit attached to the Qx and Qx backbone remain 45°, implying that the phenyl groups attached to IDT shows negligible influence on the backbone structure. **Qx3c** possesses a more planar conjugated backbone with smaller dihedral angles of 0.52° and 0.23° along the molecular backbone. Therefore, the phenyl groups attached to the IDT units prevent the intermolecular π-stacking and play a major role in impacting the molecular planarity. Figure S3 illustrates the electron distributions of their frontier molecular orbitals (LUMO and HOMO). Their HOMO levels are located on the electron-rich central part, while LUMO are concentrated onto the electron-deficient peripheral part, which will benefit charge transfer. Although the attached phenyl side groups to both IDT and Qx units cannot contribute to the electron distributions of LUMO and HOMO, the tailoring phenyl side groups slightly affect the energy levels of LUMO and HOMO due to their influence on the molecular conformations. Finally, the LUMO/HOMO energy levels of **Qx3**, **Qx3b** and **Qx3c** are calculated as −3.17 eV/−5.16 eV, −3.20 eV/−5.19 eV, −3.32 eV/−5.30 eV, respectively.

Table 1 The optoelectronic properties of **Qx3**, **Qx3b** and **Qx3c**

Compound	T_d (°C)	ε ($M^{-1}cm^{-1}$)$^{a)}$	λ_{max} (nm)		E_g (eV)$^{b)}$	HOMO (eV)$^{c)}$	LUMO (eV)$^{c)}$
			Solution	Film			
Qx3	390	1.03×10^5	613	654	1.64	−5.38	−3.56
Qx3b	385	1.04×10^5	642	706	1.59	−5.27	−3.63
Qx3c	365	1.10×10^5	636	686	1.60	−5.30	−3.59

a) Molar absorptivity at λ_{max} in solution. b) Estimated from the absorption onset in thin films. c) HOMO and LUMO energy levels were estimated from the onset oxidation and reduction potentials in the CV measurements carried out on the as-cast thin film with 0.1 mol L^{-1} Bu_4NPF_6 electrolyte acetonitrile.

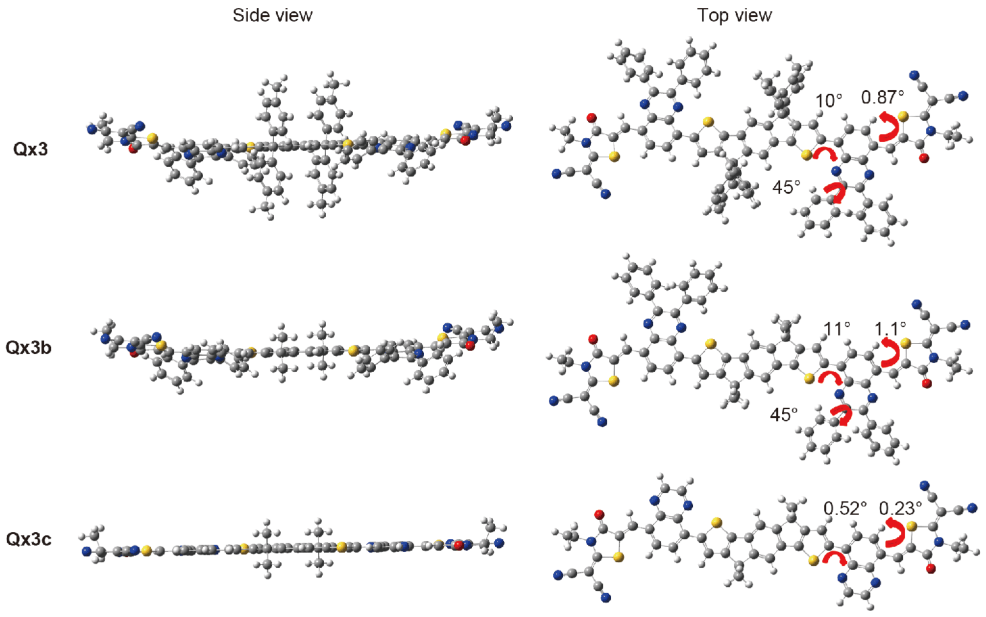

Figure 2 Side view and top view of **Qx3**, **Qx3b** and **Qx3c** optimized geometries (color online).

2.3 Photovoltaic properties

The photovoltaic performances of these new acceptors were evaluated by adopting a conventional architecture of indium tin oxide (ITO)/PEDOT:PSS/active layer/Ca/Al. The number average molecular weight (M_n) value of P3HT is 25.2 k with polydisperisity index of 2.21. In order to exploit the potentials of these new acceptors for the high performance P3HT-based OSCs, a detailed optimization was carried out through varying the weight ratio, additive and annealing temperature. These newly synthesized NFAs have good solubility in common solvents such as *o*-dichlorobenzene (ODCB), chlorobenzene (CB) and chloroform (CF), and thus the processing solvents were carefully detected. The optimal solvent was found to be ODCB and CF for P3HT:**Qx3** and P3HT:**Qx3b** devices, respectively. It is worth noting that P3HT:**Qx3c** devices exhibit quite low PCE whatever solvents are used. Taking the common additives used in P3HT-based devices into consideration, 1,8-diiodooctane (DIO), acetonitrile (CN) and diphenyl ether (DPE) were selected as the processing additives. It was found that these additives had little effect on the performance of P3HT:**Qx3** devices, but CN showed positive effect on P3HT:**Qx3b** device. The optimal D/A weight ratios were found to be 2:1 and 5:4 for P3HT:**Qx3** and P3HT:**Qx3b** devices, respectively. Upon pre-thermal annealing at 120 °C, the highest PCE was achieved for P3HT:**Qx3** devices, while the P3HT:**Qx3b** device showed the highest performance after increasing the annealing temperature to 160 °C. The average thickness of active layer of P3HT:**Qx3**, P3HT:**Qx3b** and P3HT:**Qx3c** device is 93, 114 and 101 nm, respectively. Detailed performance can be found in Figure S4.

The typical current density-voltage (*J-V*) curves are depicted in Figure 3, and the photovoltaic parameters are compiled in Table 2. After optimization, P3HT:**Qx3** device afforded an optimal PCE of 3.37% with a V_{OC} of 0.89 V, J_{SC} of 5.57 mA cm^{-2}, and fill factor (FF) of 0.68. When the phenyl side groups on the IDT unit were subtracted, the PCE of devices based on P3HT:**Qx3b** dramatically increased to 6.37%, with largely improved J_{SC} to 12.87 mA cm^{-2} and slightly decreased V_{OC} to 0.75 V and FF to 0.66. A continuous removal of phenyl side groups on the Qx units resulted in the lowest PCE of 0.03% for P3HT:**Qx3c** devices with a largely decreased J_{SC} to 0.14 mA cm^{-2} and a quite low

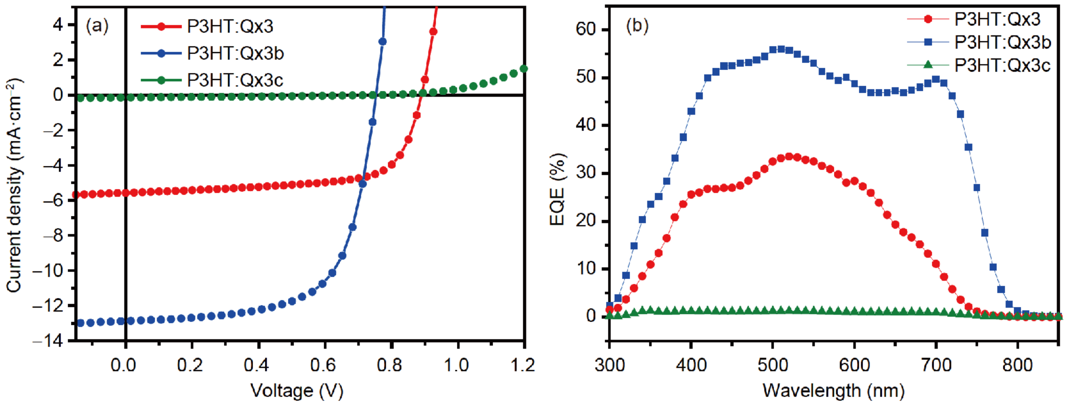

Figure 3 *J-V* characteristics (a) and EQE curves (b) of P3HT:**Qx3** (1:0.5, *w*/*w*), P3HT:**Qx3b** (1:0.8, *w*/*w*) and P3HT:**Qx3c** (1:1, *w*/*w*) devices (color online).

Table 2 Photovoltaic performance of P3HT-based OSCs under the illumination of AM 1.5 G, 100 mW cm^{-2}

Acceptor	V_{OC} (V)	J_{SC} (mA cm^{-2})	FF	PCE		μ_h (cm^2 V^{-1} s^{-1})	μ_e (cm^2 V^{-1} s^{-1})
				Best	Ave.$^{a)}$		
Qx3	0.89	5.57	0.68	3.37%	3.22%	1.1×10^{-5}	4.2×10^{-6}
Qx3b	0.75	12.87	0.66	6.37%	6.26%	1.9×10^{-4}	2.0×10^{-5}
Qx3c	0.75	0.14	0.30	0.03%	0.03%	–	1.3×10^{-4}

a) The average PCE values are calculated from eight devices.

FF to 0.30. The relatively high V_{OC} of P3HT:**Qx3** device is ascribed to the largest LUMO-HOMO offset between **Qx3** and P3HT. The removal of phenyl groups decreases V_{OC} from 0.95 to 0.75 V, which is consistent with the lower-lying LUMO energy levels of **Qx3b** and **Qx3c**. The influence of phenyl side groups on J_{SC} and FF will be discussed in the following part. Clearly, the removal of phenyl groups attached to the central IDT unit significantly enhances the PCE to 6.37%, which is one of the highest values for P3HT-based non-fullerene OSCs. The photon energy loss (E_{loss}) values are calculated by using the common formula $E_{loss}=E_g-eV_{OC}$. The E_{loss} values are 0.75, 0.84 and 0.85, respectively, which suggest there are still large room to improve the photovoltaic performance via material design.

The external quantum efficiency (EQE) curves as shown in Figure 3(b) demonstrate that P3HT:**Qx3b** devices exhibit obviously broader photocurrent response in the range of 300–800 nm than that of P3HT:**Qx3** device from 300 to 750 nm, which is consistent with their UV-vis absorption spectra of blend films as shown in Figure S5. In addition, the EQE value of P3HT:**Qx3b** is much larger than that of P3HT:**Qx3** and P3HT:**Qx3c** devices, indicating that P3HT:**Qx3b** exhibits more efficient photoelectron conversion after subtracting the phenyl side groups on IDT unit and remaining the phenyl side groups on Qx unit. The quite weak photoresponse of P3HT:**Qx3c** may be ascribed to the low hole mobility and the morphology, which will be discussed later. The maximum EQE values of **Qx3**, **Qx3b** and **Qx3c**-based devices are 34%, 57% and 1.2%, respectively. The J_{SC} values of devices calculated from integration of the EQE spectra are in good agreement with the measured J_{SC} values from *J-V*. Our results demonstrate that side chain engineering of A_2-A_1-D-A_1-A_2 type NFAs plays a vital role to affect the photocurrent response.

The exciton dissociation ability in the blend films is also probed by employing photoluminescence (PL) spectroscopy. As shown in Figure S6, when excited at 520 nm, efficient PL quenching occurred for three devices, which indicates the electron transfer from P3HT to NFA is effective. However, P3HT:**Qx3c** blend film reveals relatively incomplete PL quenching under excitation at 520 nm compared with P3HT:**Qx3** and P3HT:**Qx3b** devices. It has been accepted that the significant PL quenching of the NFA emission indicates efficient hole transfer from acceptor to P3HT through the light absorption of acceptor, which also can contribute to the current generation. Therefore, the incomplete PL quenching for P3HT:**Qx3c** might be related, at least in part, with the low J_{SC}.

In order to further understand the impact of phenyl side groups on the photovoltaic parameters J_{SC} and FF, the charge carrier (hole and electron) mobility of these systems were obtained by using the SCLC method as shown in Figure S7. The electron mobility of P3HT:**Qx3**, P3HT:**Qx3b** and P3HT:**Qx3c** systems was determined to be 4.2×10^{-6}, 2.0×10^{-5} and 1.3×10^{-4} cm^2 V^{-1} s^{-1}, respectively. Thus, it can be seen that the removing all the attached phenyl side groups increased the electron mobility, which may be ascribed to the strong intermolecular π-stacking. The hole mobility of P3HT:**Qx3** and P3HT:**Qx3b** blend was estimated to be 1.1×10^{-5} and 1.9×10^{-4} cm^2 V^{-1} s^{-1}, respectively; however the hole mobility of P3HT:**Qx3c** is so low that no SCLC region can be observed in the current density-voltage curve. Thus, P3HT:**Qx3b** exhibits relatively balanced electron and hole mobility, which is attributed to the high J_{SC} value. The relatively small J_{SC} of P3HT:**Qx3** may be ascribed to low charge carrier mobility and large overlapping light absorption with P3HT discussed above. The quite low J_{SC} and FF of P3HT:**Qx3c** device are mainly due to the unbalanced electron and hole mobility as well as the incomplete PL quenching.

2.4 Molecular orientation

The influence of phenyl side groups on the molecular packing in pristine and blend films was evaluated by two-dimensional grazing incidence wide-angle X-ray scattering (2D GIWAXS) as shown in Figure 4 and Figure S8. The scattering profiles of in-plane and out-of-plane obtained from GIWAXS patterns are shown in Figure 5. From Figure S8, the P3HT pristine thin film exhibits broad in-plane lamellar peak at 0.33 Å^{-1} (d=1.90 nm) and out-of-plane π-stacking peak at 1.75 Å^{-1} (d=0.359 nm), indicating P3HT adopts a dominant face-on orientation in thin film. For the **Qx3**, two broad scattering peaks at 0.33 and 1.25 Å^{-1} (d=0.503 nm) in the q_{xy} direction are observed in the neat film, indicating an amorphous molecular packing. The pristine film of **Qx3b** shows a lamellar peak at 0.38 Å^{-1} (d=1.65 nm) and broad scattering peak 1.69 Å^{-1} (d=0.372 nm) in the q_z direction, suggesting **Qx3b** adopts both edge-on and face-on orientation, in which the face-on packing relative to the substrate is dominant because a strong in-plane lamellar peak at 0.36 Å^{-1} (d=1.75 nm) can be also observed. **Qx3c** neat film demonstrates strong out-of-plane lamellar peak at 0.42 Å^{-1} (d=1.50 nm) and π-stacking peak at 1.81 Å^{-1} (d= 0.347 nm), therefore the crystalline **Qx3c** adopts both edge-on and face-on orientation, suggesting the removal of phenyl side groups attached on the Qx unit largely affects the molecular orientation in thin film. Compared with the GIWAXS patterns of **Qx3b** and **Qx3c**, the weaker scattering features of **Qx3** neat film suggest the lower crystallinity of **Qx3**, indicating that the substituted phenyl side groups on IDT and Qx units decreases the crystallinity. From the full width at half maximum of the (100) peak in the q_{xy} direction, their crystal coherence length values are estimated according to the Scherrer's equation [43,44], to be 10.4 nm for **Qx3**, 33.9 nm for **Qx3b** and 39.8 nm for **Qx3c** , confirming the highly crystalline **Qx3b** and **Qx3c**.

With regard to the blend films, P3HT:**Qx3** exhibits an obvious in-plane π-stacking peak at 1.66 Å^{-1} (d=0.378 nm) and an enhanced out-of-plane lamellar peak at 0.36 Å^{-1} (d= 1.75 nm) due to the overlap of the corresponding peaks of P3HT and **Qx3**, indicating that P3HT prefers an increased crystallinity and an edge-on orientation. The broad lamellar peak at 0.35 Å^{-1} and π-stacking peak at 1.25 Å^{-1} in the q_{xy} direction similar with that of **Qx3** neat film reveal that **Qx3** remains its crystalline structure after blending with P3HT, which may induce relatively large phase-separation. The clear π-stacking peak of P3HT after blending with **Qx3** also indicates a better crystalline P3HT due to the weak intermolecular interaction between P3HT and **Qx3**. For the P3HT:**Qx3b** blend film, the intensities of the in-plane lamellar peak at 0.36 Å^{-1} and the out-of-plane π-stacking peak at 1.67 Å^{-1} are enhanced, indicating P3HT and **Qx3b** adopts face-on orientation, leading to the stronger hole and electron mobility in P3HT:**Qx3b** than that of P3HT:**Qx3**. The increased intensities of the out-of-plane lamellar peak at 0.36 Å^{-1} and the in-plane lamellar peak at 0.48 Å^{-1} indicate the

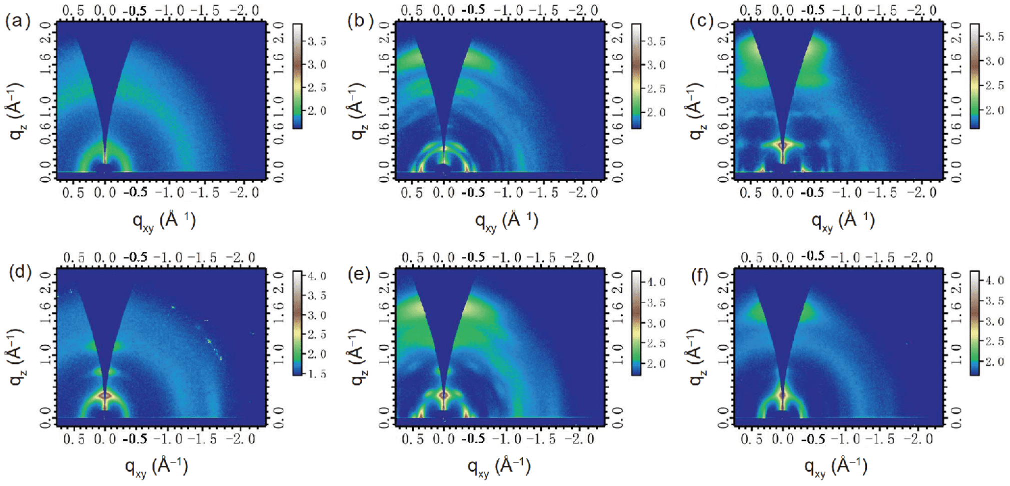

Figure 4 2D GIWAXS patterns of the pristine films of **Qx3** (a), **Qx3b** (b) and **Qx3c** (c); as well as the blend films of P3HT:**Qx3** (d), P3HT:**Qx3b** (e), and P3HT:**Qx3c** (f) (color online).

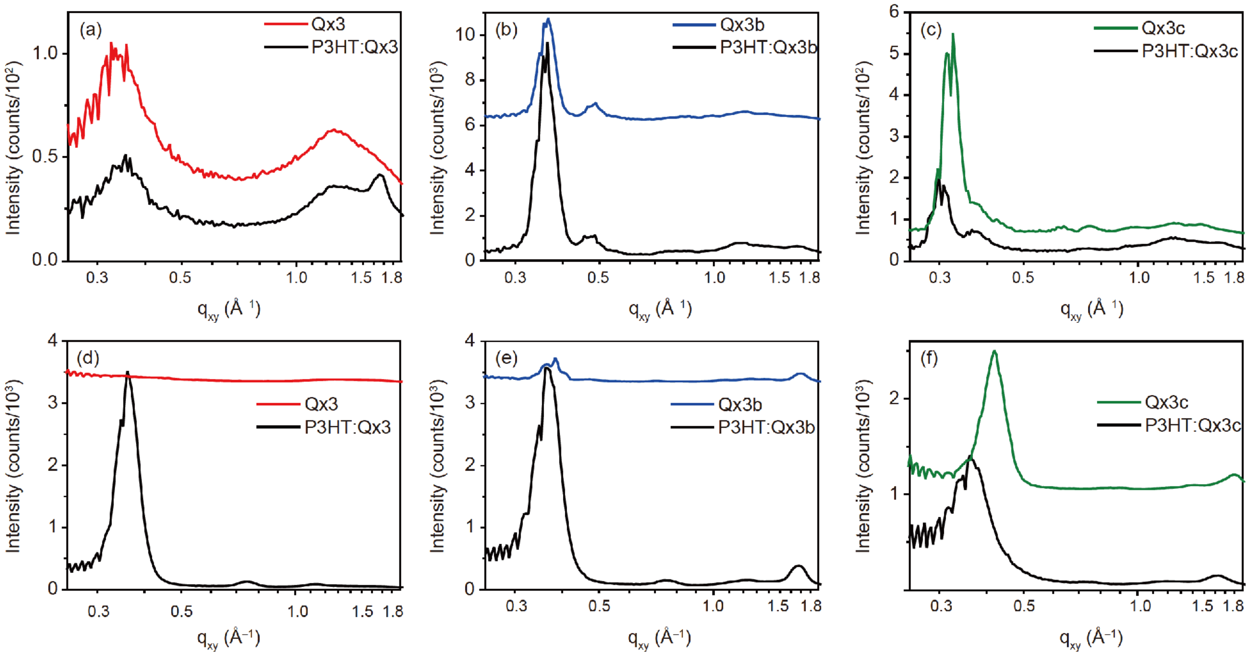

Figure 5 In-plane (a–c) and out-of-plane (d–f) GIWAXS profiles of the pristine films of **Qx3**, **Qx3b** and **Qx3c** as well as the blend films of P3HT:**Qx3**, P3HT:**Qx3b** and P3HT:**Qx3c** (color online).

stronger edge-on orientation of **Qx3b** after blending P3HT. Consequently, the largely enhanced scattering peaks of P3HT:**Qx3b** blend film compared with **Qx3b** neat film indicate the better cocrystalization of P3HT and **Qx3b** due to the strong intermolecular interaction between P3HT and **Qx3b**, which is consistent with the nanoscale phase-separation of P3HT:**Qx3b** blend film discussed later. By contrast, the P3HT:**Qx3c** blend film exhibits dramatically different scattering pattern from that of **Qx3c** neat film. The broad lamellar peak ranging from 0.275 to 0.375 Å^{-1} in the q_{xy} direction becomes weakened and narrowed to a range of 0.275–0.32 Å^{-1}, suggesting that P3HT adopts the amorphous structure due to the absence of lamellar peak at 0.33 Å^{-1}. In the q_z direction, the lamellar peak at 0.42 Å^{-1} and π-stacking peak at 1.80 Å^{-1} down-shift to 0.36 and 1.66 Å^{-1}, respectively, indicating that the introduction of P3HT not only decreases the crystallinity of **Qx3c** but also increases the lamellar and π-stacking distance. The highly crystalline **Qx3c** domain in the P3HT:**Qx3c** blend film leads to high electron mobility. However the serious imbalance hole/electron mobility results in quite low J_{SC} and FF.

In short, a large fraction of face-on orientation in P3HT:**Qx3b** blend film is benefit for the vertical charge transport, while the edge-on orientation in P3HT:**Qx3** and P3HT:**Qx3c** blend film is detrimental to the charge transport. Therefore, the removal of phenyl side groups attached to the Qx unit properly regulates the morphological properties of active layers, while the absence of phenyl side groups possibly induces excessive aggregation due to the weak steric hindrance effect.

2.5 Film morphology

Atomic force microscopy (AFM) was employed to understand the impact of phenyl side groups on the morphology of the blend films, which not only revealed the molecular crystallinity but also explained the charge transport property through the phase-separation size. The height and phase images of blend films were obtained from AFM characterizations as shown in Figure 6. Compared with P3HT:**Qx3** blend film exhibiting large phase separation with a root-mean-square roughness (RMS) value of 5.93 nm, P3HT:**Qx3b** shows a nanoscale homogeneous surface with a RMS of 1.84 nm, indicating that subtraction of phenyl groups from the IDT core unit dramatically increases the miscibility between P3HT and acceptor, which may also induce the enhancement of light harvesting of blend film [45]. The relatively larger RMS of P3HT:**Qx3** blend film may be ascribed to the steric molecular geometry of **Qx3** due to the presence of eight phenyl side groups, which prevents the formation of bicontinuous interpenetrating structure. By contrast, P3HT:**Qx3c** blend film exhibits obviously large aggregations unevenly distributed on the surface because of the planar molecular conformation. The optical microscopy images as shown in Figure 7 also reveal much smoother surface of P3HT:**Qx3** and P3HT:**Qx3b** blend film as well as an excessive aggregation in P3HT:**Qx3c** blend film. Notice that the poor morphology of P3HT:**Qx3c** cannot be further improved by the solvent additive and annealing temperature. Therefore, other donor materials with a strong intermolecular force to **Qx3c** might be suitable for the absorption and en-

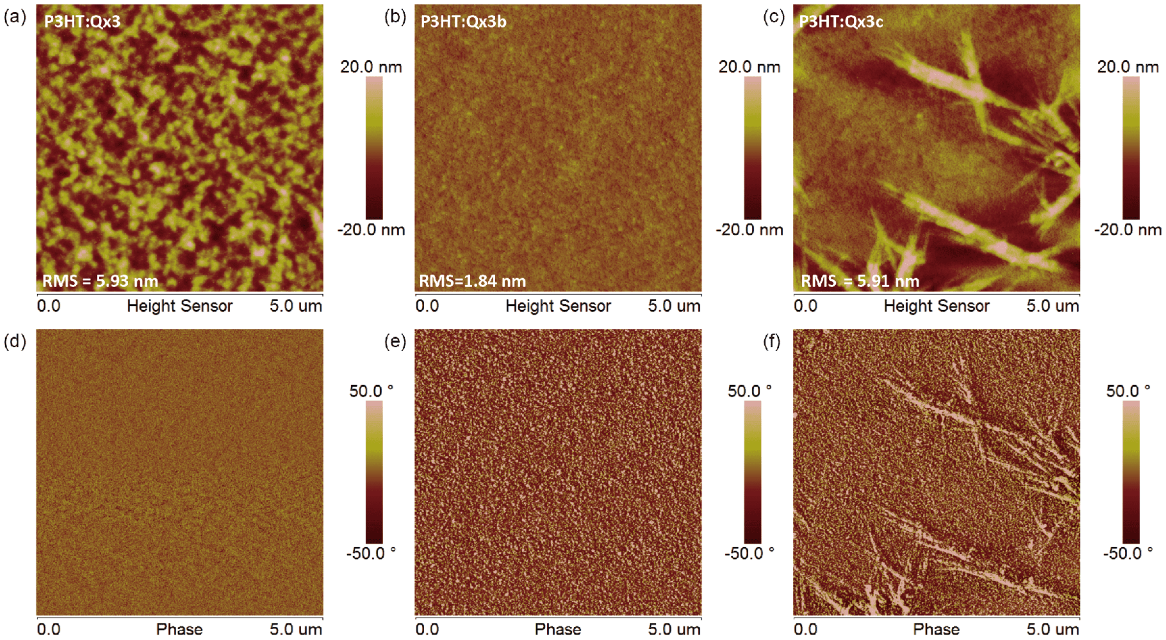

Figure 6 AFM height (top) and phase (bottom) images (5 μm×5 μm) of P3HT:**Qx3** (a, d), P3HT:**Qx3b** (b, e) and P3HT:**Qx3c** (c, f) (color online).

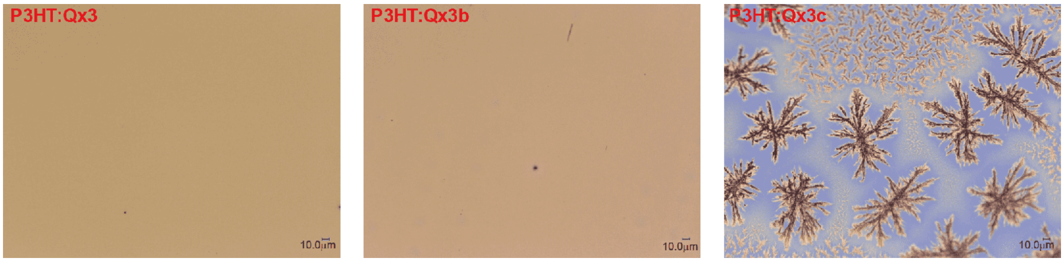

Figure 7 Optical microscopy images of P3HT:**Qx3**, P3HT:**Qx3b** and P3HT:**Qx3c** blend films (color online).

ergy level matching.

3 Conclusions

In summary, we designed three kinds of Qx-based non-fullerene molecules, **Qx3**, **Qx3b** and **Qx3c**, in order to pursue suitable acceptors matching with the traditional p-type polymer P3HT. After sequential tailoring the phenyl side groups attached to the molecular main chain, their optical, electronic, crystallinity, charge-transport and photovoltaic properties are systematically investigated. Compared with parent **Qx3**, **Qx3b** shows a red-shifted absorption, a decreased LUMO level, an increased HOMO level and finally a reduced bandgap after removal of four phenyl groups attached to the IDT core. The continuous tailoring four phenyl rings on the Qx resulted in **Qx3c** possessing a slightly blue-shifted absorption, a slight increased LUMO level and decreased HOMO level in comparison with **Qx3b**. The theoretical calculation further confirms that the effects of phenyl groups attached to IDT and Qx on molecular conformations and electronic properties are different. The attached phenyl groups decrease the miscibility of **Qx3** with P3HT, leading to a large phase-separation in the P3HT:**Qx3** blend film. **Qx3b** has better cocrystallization with P3HT and shows enhanced face-on molecular orientation, which thus facilitate the improvement of J_{SC}. The absence of phenyl groups on both IDT and Qx increases the molecular planarity but leads to excessive aggregation of **Qx3c** in the blend film. The P3HT:**Qx3b** device shows the highest PCE of 6.37%, which is one of the currently reported top PCE of P3HT-based devices with non-fullerene acceptors. The results indicate that side chain engineering plays a vital role to A_2-A_1-D-A_1-A_2 type NFAs to balance the miscibility and crystallinity with P3HT for achieving bicontinuous interpenetrating network in active layers. In additions, our works also prove that Qx unit is also an effective electron-deficient building block, like traditional BT and BTA, to construct NFAs to combine with P3HT.

Acknowledgements This work was supported by the Key Research Program of Frontier Sciences, Chinese Academy of Sciences (QYZDB-SSW-SLH033), the National Key Research and Development Program of China (2017YFA0206600) and the National Natural Science Foundation of China (51673048, 21875052, 51773046, 21602040, 51873044).

Supporting information The supporting information is available online at http://chem.scichina.com and http://link.springer.com/journal/11426. The supporting materials are published as submitted, without typesetting or editing. The responsibility for scientific accuracy and content remains entirely with the authors.

1 Yu G, Gao J, Hummelen JC, Wudl F, Heeger AJ. *Science*, 1995, 270: 1789–1791
2 Yan C, Barlow S, Wang Z, Yan H, Jen AKY, Marder SR, Zhan X. *Nat Rev Mater*, 2018, 3: 18003
3 Tang A, Zhan C, Yao J, Zhou E. *Adv Mater*, 2017, 29: 1600013
4 Geng Y, Tang A, Tajima K, Zeng Q, Zhou E. *J Mater Chem A*, 2019, 7: 64–96
5 Yang J, Xiao B, Tang A, Li J, Wang X, Zhou E. *Adv Mater*, 2018, 4: 1804699
6 Li G, Shrotriya V, Huang J, Yao Y, Moriarty T, Emery K, Yang Y. *Nat Mater*, 2005, 4: 864–868
7 Fan B, Zhang D, Li M, Zhong W, Zeng Z, Ying L, Huang F, Cao Y. *Sci China Chem*, 2019, 62: 746–752
8 Hildner R, Köhler A, Müller-Buschbaum P, Panzer F, Thelakkat M. *Adv Energy Mater*, 2017, 7: 1700314
9 Po R, Bernardi A, Calabrese A, Carbonera C, Corso G, Pellegrino A. *Energy Environ Sci*, 2014, 7: 925–943
10 Liu Y, Summers MA, Edder C, Fréchet JMJ, McGehee MD. *Adv Mater*, 2005, 17: 2960–2964
11 Guo X, Cui C, Zhang M, Huo L, Huang Y, Hou J, Li Y. *Energy Environ Sci*, 2012, 5: 7943
12 Zhai W, Tang A, Xiao B, Wang X, Chen F, Zhou E. *Sci Bull*, 2018, 63: 845–852
13 Mahmood A, Yang J, Hu J, Wang X, Tang A, Geng Y, Zeng Q, Zhou E. *J Phys Chem C*, 2018, 122: 29122–29128
14 Yang L, Gu W, Lv L, Chen Y, Yang Y, Ye P, Wu J, Hong L, Peng A, Huang H. *Angew Chem Int Ed*, 2018, 57: 1096–1102
15 Yuan J, Zhang Y, Zhou L, Zhang G, Yip HL, Lau TK, Lu X, Zhu C, Peng H, Johnson PA, Leclerc M, Cao Y, Ulanski J, Li Y, Zou Y. *Joule*, 2019, 3: 1140–1151
16 Yang J, Cong P, Chen L, Wang X, Li J, Tang A, Zhang B, Geng Y, Zhou E. *ACS Macro Lett*, 2019, 8: 743–748
17 Chen Y, Geng Y, Tang A, Wang X, Sun Y, Zhou E. *Chem Commun*, 2019, 55: 6708–6710
18 Winzenberg KN, Kemppinen P, Scholes FH, Collis GE, Shu Y, Birendra Singh T, Bilic A, Forsyth CM, Watkins SE. *Chem Commun*, 2013, 49: 6307–6309
19 Holliday S, Ashraf RS, Nielsen CB, Kirkus M, Röhr JA, Tan CH, Collado-Fregoso E, Knall AC, Durrant JR, Nelson J, McCulloch I. *J Am Chem Soc*, 2015, 137: 898–904
20 Kim Y, Song CE, Moon SJ, Lim E. *Chem Commun*, 2014, 50: 8235–8238
21 Lin Y, Li Y, Zhan X. *Adv Energy Mater*, 2013, 3: 724–728
22 Gupta A, Rananaware A, Srinivasa Rao P, Duc La D, Bilic A, Xiang W, Li J, Evans RA, Bhosale SV, Bhosale SV. *Mater Chem Front*, 2017, 1: 1600–1606
23 Yan Q, Zhou Y, Zheng YQ, Pei J, Zhao D. *Chem Sci*, 2013, 4: 4389–4394
24 Liu F, Zhou Z, Zhang C, Vergote T, Fan H, Liu F, Zhu X. *J Am Chem Soc*, 2016, 138: 15523–15526
25 Qiu N, Yang X, Zhang H, Wan X, Li C, Liu F, Zhang H, Russell TP, Chen Y. *Chem Mater*, 2016, 28: 6770–6778
26 Baran D, Ashraf RS, Hanifi DA, Abdelsamie M, Gasparini N, Röhr JA, Holliday S, Wadsworth A, Lockett S, Neophytou M, Emmott CJM, Nelson J, Brabec CJ, Amassian A, Salleo A, Kirchartz T, Durrant JR, McCulloch I. *Nat Mater*, 2017, 16: 363–369
27 Wu Y, Bai H, Wang Z, Cheng P, Zhu S, Wang Y, Ma W, Zhan X. *Energy Environ Sci*, 2015, 8: 3215–3221
28 Holliday S, Ashraf RS, Wadsworth A, Baran D, Yousaf SA, Nielsen CB, Tan CH, Dimitrov SD, Shang Z, Gasparini N, Alamoudi M, Laquai F, Brabec CJ, Salleo A, Durrant JR, McCulloch I. *Nat Commun*, 2016, 7: 11585
29 Xiao B, Tang A, Zhang J, Mahmood A, Wei Z, Zhou E. *Adv Energy Mater*, 2017, 7: 1602269
30 Xiao B, Tang A, Yang J, Wei Z, Zhou E. *ACS Macro Lett*, 2017, 6: 410–414
31 Tang A, Xiao B, Wang Y, Gao F, Tajima K, Bin H, Zhang ZG, Li Y, Wei Z, Zhou E. *Adv Funct Mater*, 2018, 28: 1704507
32 Tang A, Xiao B, Chen F, Zhang J, Wei Z, Zhou E. *Adv Energy Mater*, 2018, 8: 1801582
33 Xiao B, Tang A, Cheng L, Zhang J, Wei Z, Zeng Q, Zhou E. *Sol RRL*, 2017, 1: 1700166
34 Xiao B, Tang A, Zhang Q, Li G, Wang X, Zhou E. *ACS Appl Mater Interfaces*, 2018, 10: 34427–34434
35 Yuan J, Ouyang J, Cimrová V, Leclerc M, Najari A, Zou Y. *J Mater Chem C*, 2017, 5: 1858–1879
36 Gedefaw D, Prosa M, Bolognesi M, Seri M, Andersson MR. *Adv Energy Mater*, 2017, 7: 1700575
37 Liu M, Gao Y, Zhang Y, Liu Z, Zhao L. *Polym Chem*, 2017, 8: 4613–4636
38 Xiao B, Tang A, Yang J, Mahmood A, Sun X, Zhou E. *ACS Appl Mater Interfaces*, 2018, 10: 10254–10261
39 Wang T, Lau TK, Lu X, Yuan J, Feng L, Jiang L, Deng W, Peng H, Li Y, Zou Y. *Macromolecules*, 2018, 51: 2838–2846
40 Zheng Z, Awartani OM, Gautam B, Liu D, Qin Y, Li W, Bataller A, Gundogdu K, Ade H, Hou J. *Adv Mater*, 2017, 29: 1604241
41 Chen W, Salim T, Fan H, James L, Lam YM, Zhang Q. *RSC Adv*, 2014, 4: 25291–25301
42 Qi X, Lo YC, Zhao Y, Xuan L, Ting HC, Wong KT, Rahaman M, Chen Z, Xiao L, Qu B. *Front Chem*, 2018, 6: 260
43 Rivnay J, Noriega R, Kline RJ, Salleo A, Toney MF. *Phys Rev B*, 2011, 84: 045203
44 Zhu C, Zhao Z, Chen H, Zheng L, Li X, Chen J, Sun Y, Liu F, Guo Y, Liu Y. *J Am Chem Soc*, 2017, 139: 17735–17738
45 Bi YG, Feng J, Ji JH, Yi FS, Li YF, Liu YF, Zhang XL, Sun HB. *Nanophotonics*, 2017, 7: 60